Check for updates

Electrical field and biaxial strain tunable electronic properties of the PtSe₂/Hf₂CO₂ heterostructure†

Ruizhe Xia, [ID] Yi Peng, Li Fang [ID] * and Xuan Meng

The structure and electronic properties of two-dimensional vertical van der Waals PtSe₂/Hf₂CO₂ heterostructure have been investigated based on first-principles calculations. The results show that the PtSe₂ and Hf₂CO₂ monolayers form a type-I heterostructure with both the conduction band minimum (CBM) and valence band maximum (VBM) located at the Hf₂CO₂ layer. The electronic properties of PtSe₂/Hf₂CO₂ heterostructure can be effectively adjusted by applying external electric field or biaxial strain. The transition in band alignment from type-I to type-II can be manipulated by controlling the strength and direction of the electric field. Additionally, the transition from type-I to type-II have also taken place under the strains, and the band gap of the PtSe₂/Hf₂CO₂ heterostructure decreases with increasing the compressive or tensible strain. Under a strong strain of −8%, the PtSe₂/Hf₂CO₂ heterostructure can transform from semiconductor to metal. These findings provide a promising method to tune the electronic properties of PtSe₂/Hf₂CO₂ heterostructure and design a new vdW heterostructure in the applications for electronic and optoelectronic devices.

1. Introduction

Two-dimensional (2D) van der Waals (vdW) materials with atomic layer thickness and tunable band gap have attracted great attention.[1,2] van der Waals heterostructures, fabricated by vertically stacking two different 2D materials together,[3–5] not only maintain the individual electronic properties of each material because of the weak interaction between layers, but also have some new physics at the interface,[6] which offer a novel platform for innovative devices and applications, such as solar cells,[7] tunneling transistor memory devices,[8] *etc.* According to the band alignment, the vdW heterostructures can be classified as three types: type-I (straddling gap), type-II (staggered gap), and type-III (broken gap).[9] In type-I heterostructures, both the conduction band minimum (CBM) and the valence band maximum (VBM) are located in the same material with the narrower bandgap. The quantum confinement of electrons and holes in the same region facilitates their radiative recombination, which is desirable in light-emitting-diodes (LEDs).[10] For type-II heterostructure, the CBM and VBM exist in different layers, where the electrons and holes are spatially separated, thereby greatly decreasing the probability of recombination and facilitating efficient electron–hole separation for light detection and harvesting, which are highly desirable for photocatalytic and photovoltaic devices.[11,12] Different from type-I and type-II

heterostructures, for type-III heterostructures, the VBM and CBM of one layer are both above the CBM of the other one,[13] enabling a nonoverlapping band offset between two semiconductors that facilitates the transport of charge carriers from one energy band to another *via* a quantum tunneling process.[14,15] This band-to-band tunneling (BTBT) makes type-III vdW heterostructures well-suited for tunnel devices with high-speed operation and low-power consumption, such as TFETs or Esaki diodes.[16] Notably, the types and the electronic properties of vdW heterostructure can be modulated by various methods, such as coupling interlayer distances,[17] applying external electric fields,[18] and applying biaxial strain,[19] to obtain unique structures and performances. These charming findings suggest that stacking 2D materials into vdW heterostructures provides an effective way to design novel artificial materials with special characteristics.

Since Yury Gogotsi *et al.* successfully synthesized Mxenes in 2011,[20] the 2D MXene have attracted much interest from researchers, owing to its unique physicochemical characteristics and wide range of applications in supercapacitors,[21] batteries,[22] sensors,[23] catalysis,[24] optoelectronics.[25] Hf₂CO₂ is a classical MXene with a band gap of 1.0 eV (PBE) and 1.75 eV (HSE06).[26] It has a low thermal expansion coefficient, high carrier mobility, and high thermal conductivity,[27] which make it have promising applications in optoelectronics,[28] solar cells,[29] and gas sensors.[30] Inheriting the properties of isolated Hf₂CO₂, the Hf₂CO₂-based vdW heterostructures for opto-electronic device applications have also been investigated extensively. For example the Hf₂CO₂/MoS₂,[31] Hf₂CO₂/WS₂,[32] and Hf₂CO₂/GaN[33] vdW heterostructures have been

School of Science, Hubei University of Technology, Wuhan 430068, P. R. China. E-mail: fangli@hbut.edu.cn

suggested as potential photocatalysts for overall water splitting with appropriate band structure and high carrier mobility.

PtSe$_2$, as one kind of transition-metal dichalcogenide (TMDC), has attracted intense interest. It has a graphene-like structure with high stability[34] semimetallic electronic structures, and excellent photoelectric properties.[35] Additionally, external electric field[36] and strain[37] can effectively regulate its electronic properties, and make the indirect–direct bandgap transition and semiconductor-semimetal transition happen. These excellent characteristics of PtSe$_2$ monolayer have enabled its potential applications in various devices, including field effect transistors, gas sensors, and photocatalysts.[38–41]

Although the preliminary researches on the electronic properties of the Hf$_2$CO$_2$-based and PtSe$_2$-based vdW heterostructures have maken great progresses, the study on the properties of PtSe$_2$/Hf$_2$CO$_2$ vdW heterostructure is very scarce. Therefore, in this work, the PtSe$_2$/Hf$_2$CO$_2$ heterostructure has been investigated *via* first-principles calculations. The effects of stacking pattern, external electric field, and biaxial strain on the electronic properties of the PtSe$_2$/Hf$_2$CO$_2$ vdW heterostructure were discussed. Our research results show that the PtSe$_2$/Hf$_2$CO$_2$ vdW heterostructure exhibits a type-I band alignment (straddling gap), which can offer the application for LEDs. We have also found that the applied external electric fields and biaxial strains are efficient means ofor adjusting its electronic properties, which can broaden the application of PtSe$_2$/Hf$_2$CO$_2$ vdW heterostructure. Our results are expected to provide theoretical guidance for the design of flexible nano-electronic or optoelectronic devices based on the PtSe$_2$/Hf$_2$CO$_2$ vdW heterostructure.

2. Computational method

All structure relaxations and electronic property calculations in our work were performed using density functional theory (DFT)[42] in conjunction with plane-wave ultrasoft pseudopotential, as implemented in the Vienna *ab initio* simulation package (VASP).[43] The generalized gradient approximation (GGA) of the Perdew–Burke–Ernzerhof (PBE) function was employed to express the exchange–correlation energy.[44] The cut-off energy was set to 500 eV, and the first Brillouin zone sampling was carried out by using $4 \times 4 \times 1$ for structure optimization and using $6 \times 6 \times 1$ for electronic properties calculations, respectively. The lattice parameters and ionic positions were fully relaxed until the total energies and forces were less than 10^{-6} eV and 0.02 eV Å^{-1}, respectively. To avoid spurious interactions between periodic neighbour structures, a vacuum thickness of 20 Å was chosen. Besides, a dispersion-corrected DFT method of Grimme (DFT-D3) was employed to correctly describe the effect of a vdW interaction.[45] As the PBE functional usually underestimates the band gap value, the Heyd–Scuseria–Ernzerhof (HSE06) hybrid functional was adopted for comparison.

3. Results and discussions

3.1. The pristine PtSe$_2$ and Hf$_2$CO$_2$ monolayers

Fig. 1a and b display the optimized structures of individual PtSe$_2$ and Hf$_2$CO$_2$ single layers. The relaxed lattice parameters of the pristine PtSe$_2$ and Hf$_2$CO$_2$ monolayers are 3.745 and 3.265 Å, respectively, which very well agree with the values in earlier theoretical and experimental findings.[32,37] The energy
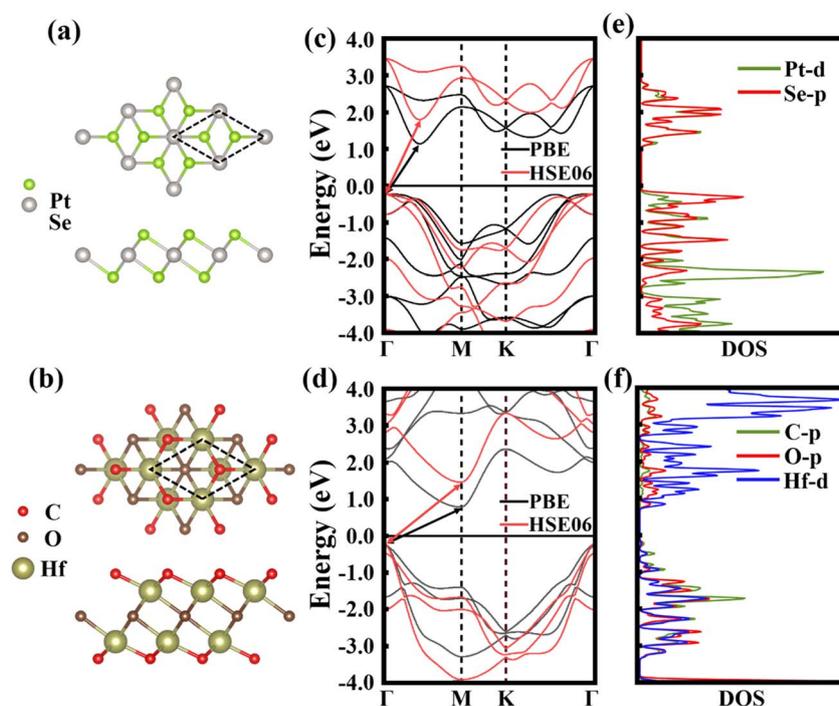

Fig. 1 (a) and (b) Top and side views of PtSe$_2$ and Hf$_2$CO$_2$ monolayers. (c) and (d) The band structures calculated by the PBE and HSE06 methods, respectively. (e) and (f) Corresponding partial densities of states (PDOS) of the primitive cells of PtSe$_2$ and Hf$_2$CO$_2$ monolayers, calculated by PBE method.
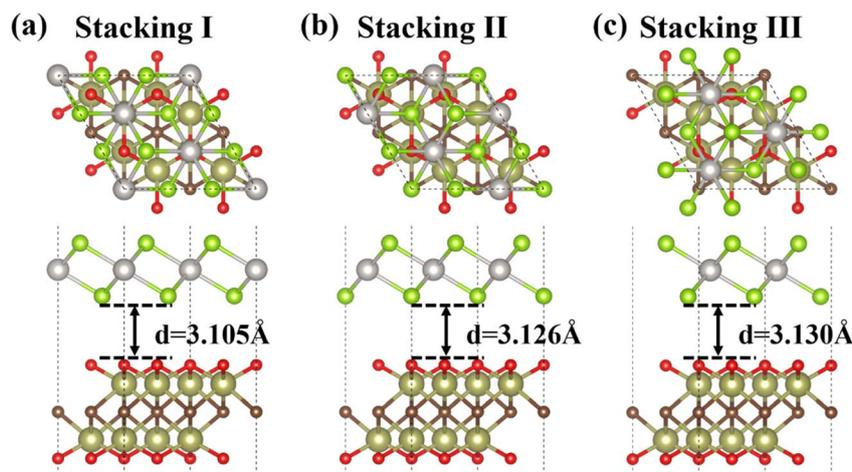
Fig. 2 Top and side views of three different stacking configurations of the PtSe$_2$/Hf$_2$CO$_2$ heterostructure: (a) stacking I, (b) stacking II, (c) stacking III.

Table 1 Lattice parameter (a), bond length (L_{x-x}), band energy (E_g), interlayer distance (d) and binding energy (E_b)

System	Type	a (Å)	L_{Pt-Se} (Å)	L_{Hf-O} (Å)	L_{Hf-C} (Å)	PBE/HSE06 E_g (eV)	d (Å)	E_b (meV Å^{-2})
PtSe$_2$	—	3.748	2.528	—	—	1.398/1.990	—	—
Hf$_2$CO$_2$	—	3.265	—	2.100	2.335	0.988/1.749	—	—
PtSe$_2$/Hf$_2$CO$_2$	I	6.492	2.529	2.096	2.324	0.965/1.788	3.105	−23.082
	II	6.491	2.529	2.094	2.328	0.964/—	3.126	−22.959
	III	6.491	2.530	2.094	2.327	0.957/—	3.130	−22.887

band structures of pristine PtSe$_2$ and Hf$_2$CO$_2$ monolayers are shown in Fig. 1c and d. Both PtSe$_2$ and Hf$_2$CO$_2$ monolayers exhibit indirect band gaps of 1.398/1.990 eV and 0.988/1.749 eV calculated by PBE/HSE06 functionals, respectively. The valence band maximum (VBM) and conduction band minimum (CBM) of PtSe$_2$ are located at Γ and Γ–M, respectively, while the VBM and CBM of Hf$_2$CO$_2$ are located at Γ and M, respectively. Fig. 1e demonstrates that in the PtSe$_2$ monolayer, the CBM is mainly contributed by the Se-p and Pt-d states, while the VBM is largely contributed by the Se-p state. Fig. 1f shows that in the Hf$_2$CO$_2$

monolayer, the VBM is contributed by Hf-d state, and the CBM is primarily contributed by the C-p state. These calculated outcomes are consistent with previous studies.[32,33,46,47]

3.2. Structural and electronic properties of PtSe$_2$/Hf$_2$CO$_2$ vdW heterostructures

The $\sqrt{3} \times \sqrt{3}$ supercell of PtSe$_2$ and 2 × 2 supercell of Hf$_2$CO$_2$ are used to construct the PtSe$_2$/Hf$_2$CO$_2$ heterostructure. The lattice mismatch is only 0.29%, making it more possible to
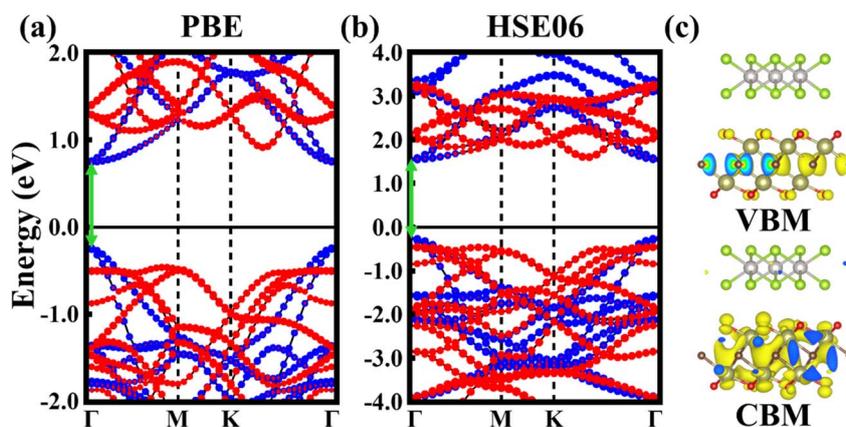

Fig. 3 (a) and (b) The projected band structures of PtSe$_2$/Hf$_2$CO$_2$ heterostructure calculated by PBE and HSE06 method, respectively, the Fermi level is set as zero, the red and blue lines represent PtSe$_2$ and Hf$_2$CO$_2$, respectively. (c) The partial charge densities corresponding to the VBM and CBM of the PtSe$_2$/Hf$_2$CO$_2$ heterostructure.

Table 2 Edges of VBM and CBM and work function for materials

System		VBM (eV)	CBM (eV)	Work function (eV)
Isolated	PtSe$_2$	−4.25	−6.24	6.03
	Hf$_2$CO$_2$	−4.28	−0.68	5.67
PtSe$_2$/Hf$_2$CO$_2$	PtSe$_2$	−4.28	−6.08	5.83
	Hf$_2$CO$_2$	−4.23	−6.29	

achieve experimental synthesis of the PtSe$_2$/Hf$_2$CO$_2$ hetero-structure. In Fig. 2, three distinct stacking configurations of PtSe$_2$/Hf$_2$CO$_2$ heterostructure were studied. These configurations were created by shifting the relative positions of two layers in the horizontal direction. The binding energy E_b were calculated to estimate the thermodynamic stability of the system. It is defined as follows:

$$E_b = [(E_{total} − E_{PtSe_2} − E_{Hf_2CO_2})/S] \quad (1)$$

where E_{total}, E_{PtSe_2} and $E_{Hf_2CO_2}$ represent the total energy of the heterostructure, PtSe$_2$ monolayer, and Hf$_2$CO$_2$ monolayer, respectively, and S is the interface area of the heterostructure. The optimized lattice parameters, interlayer distances, bond lengths, and calculated binding energies are listed in Table 1. The results demonstrated no significant variation in the bond length of these three structures, and the interlayer distances are approximately 3.1 Å. The calculated binding energies E_b are −23.082, −22.959 and −22.887 meV Å^{-2} for stacking I, II, and III patterns, respectively, which are lower than PtSe$_2$/GaN, PtSe$_2$/Arsenene, and *etc.*,[48–53] confirming that PtSe$_2$/Hf$_2$CO$_2$ bilayer forms a stable vdW heterostructure. In addition, the band gaps of stacking I to III are 0.965, 0.964, and 0.957 eV respectively, calculated by the PBE method, as shown in Fig. S2.† Therefore, it can be concluded that the structural and electronic properties of PtSe$_2$/Hf$_2$CO$_2$ vdW heterostructure are not sensitive to diverse stacking patterns. For the ease of analysis, stacking I has been selected for subsequent calculations due to its relatively small binding energy.

Fig. 3a and b show the band structures of the PtSe$_2$/Hf$_2$CO$_2$ heterostructure with stacking I configuration, calculated by the PBE/HSE06 functional. Both the CBM and the VBM are

contributed by Hf$_2$CO$_2$ layer. The band gap of the hetero-structure is respectively 0.965/1.788 eV using PBE/HSE06 functional. Fig. 3c displays the band-resolved charge densities of the CBM and VBM for the PtSe$_2$/Hf$_2$CO$_2$ vdW heterostructure. The results indicate that the PtSe$_2$/Hf$_2$CO$_2$ vdW heterostructure exhibits a type-I band alignment. Besides, we found that the PBE functional has indeed underestimated the band gap value, but the band structure obtained from PBE has almost exhibited the same trend to that obtained from HSE06 functional.

Next, the work function is employed to deeply understand the band alignment of the PtSe$_2$/Hf$_2$CO$_2$ vdW heterostructure. The definition of work function (Φ) is

$$\Phi = E_{vac} − E_F \quad (2)$$

where E_{vac} and E_F represent the vacuum level and Fermi level, respectively. The calculated work function of the PtSe$_2$ layer and the Hf$_2$CO$_2$ layer are 6.03 and 5.67 eV, respectively, shown in Table 2. The electrons move from Hf$_2$CO$_2$ layer to the PtSe$_2$ layer due to the smaller work function of Hf$_2$CO$_2$ layer, resulting in an electric field (E_{in}) in the interlayer, which, in turn, impedes the transfer of charge and ultimately establishes an electrostatic equilibrium, as shown in Fig. 4a. As a result of charge transfer, the Fermi level of the PtSe$_2$ layer moves up while the Fermi level of the Hf$_2$CO$_2$ layer goes down for equilibrium Fermi level. Consequently, the work function of the heterostructure is calculated to be 5.83 eV.

To visualize the charge transfer and charge redistribution, the differential charge density ($\Delta\rho$) have been studied. The $\Delta\rho$ was determined as:

$$\Delta\rho = \rho_{PtSe_2/Hf_2CO_2} − \rho_{PtSe_2} − \rho_{Hf_2CO_2} \quad (3)$$

where ρ_{PtSe_2/Hf_2CO_2}, ρ_{PtSe_2}, and $\rho_{Hf_2CO_2}$ are the charge densities of the PtSe$_2$/Hf$_2$CO$_2$ heterostructure and isolated PtSe$_2$ and Hf$_2$CO$_2$ monolayers, respectively. The 3D charge density difference is depicted in Fig. 4b, with the cyan area signifying electron gain and the yellow area signifying electron loss. The electrons and holes are located on the PtSe$_2$ layer and Hf$_2$CO$_2$ layer, respectively. The planar-averaged differential charge density is described in Fig. 4c. Positive and negative values reflect charge accumulation and depletion, respectively. At the
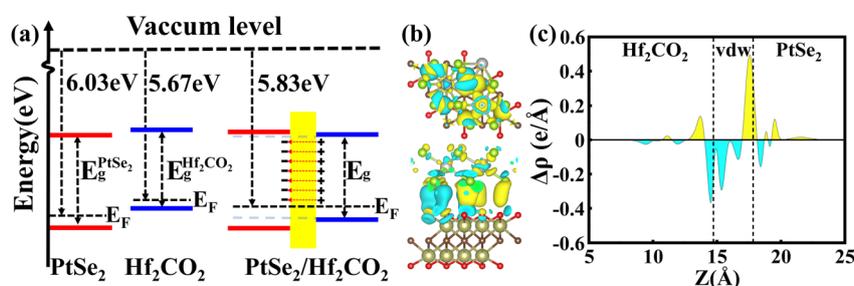

Fig. 4 (a) The band alignment of PtSe$_2$/Hf$_2$CO$_2$ vdW heterostructure. $E_g^{PtSe_2}$, $E_g^{Hf_2CO_2}$ and E_g are the band gaps of PtSe$_2$ layer, Hf$_2$CO$_2$ layer and PtSe$_2$/Hf$_2$CO$_2$ heterostructure, respectively. (b) The side and top views of the 3D isosurface with charge density difference for PtSe$_2$/Hf$_2$CO$_2$ heterostructure. The cyan and yellow regions represent the electrons depletion and accumulation, respectively. The charge density value corresponding to the isosurfaces drawn is 0.805e Å^{-3}. (c) The planar-averaged charge density difference for PtSe$_2$/Hf$_2$CO$_2$ heterostructure.

surface of PtSe$_2$/Hf$_2$CO$_2$ heterostructure, electrons acculmulated on the PtSe$_2$ side and depleted on the Hf$_2$CO$_2$ side, indicating electron transfer from the Hf$_2$CO$_2$ layer to the PtSe$_2$ layer after the two layers contact.

3.3. Effect of external electric field

In order to explore the possible application of the PtSe$_2$/Hf$_2$CO$_2$ vdW heterostructure, we have modulated the electronic properties by applying external electric field. Considering that
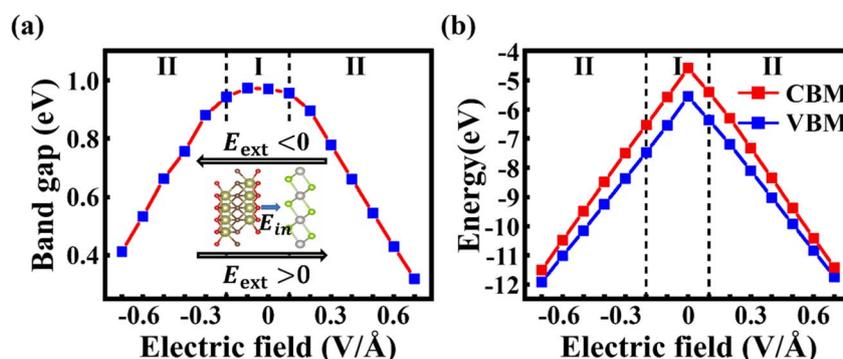

Fig. 5 (a) The band gap evolution of PtSe$_2$/Hf$_2$CO$_2$ heterostructure as a function of E_{ext}. The inset shows directions of build-in electric field, negative and positive external electric field. (b) The band edge evolution of PtSe$_2$/Hf$_2$CO$_2$ heterostructure as a function of E_{ext}.
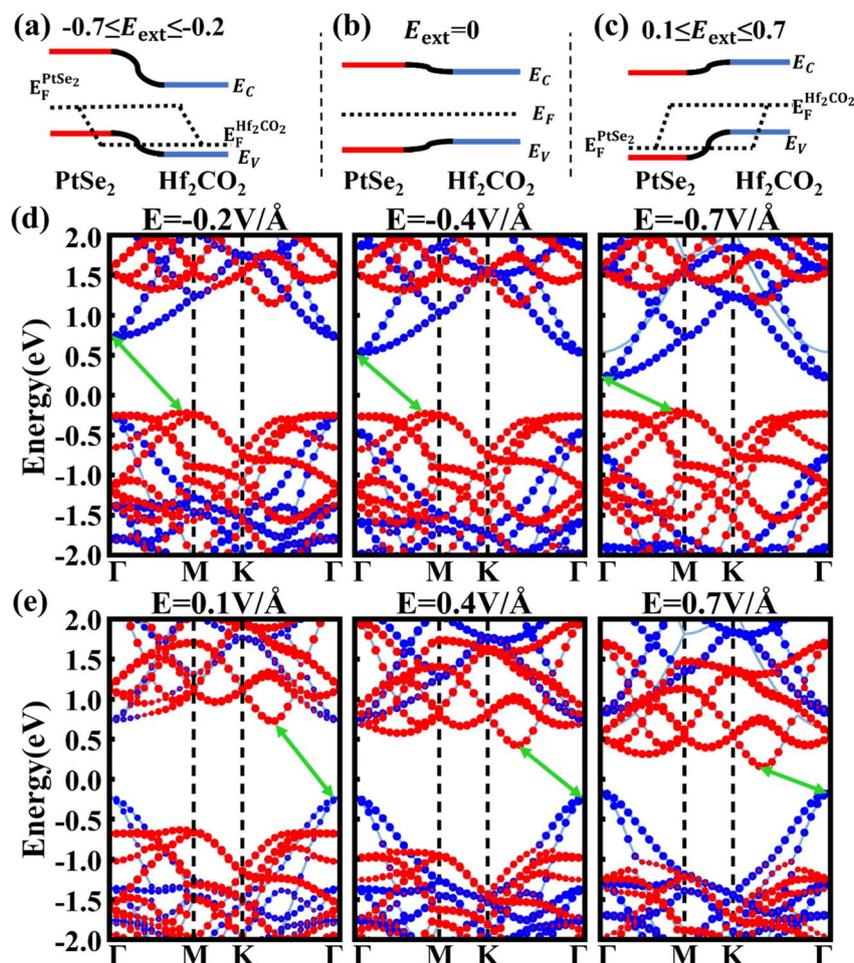

Fig. 6 (a) Type-II band alignment under a negative external electric field. (b) Type-I band alignment without an external electric field, and (c) Type-II band alignment under a positive external electric field. $E_F^{PtSe_2}$ and $E_F^{Hf_2CO_2}$ are the quasi-Fermi levels of PtSe$_2$ and Hf$_2$CO$_2$ layers in the heterostructure, respectively. (d), (e) The band structures of PtSe$_2$/Hf$_2$CO$_2$ heterostructure under the negative of −0.2, −0.4 and −0.7 V Å^{-1}, and positive electric fields of 0.1, 0.4 and 0.7 V Å^{-1}, respectively, where the red and blue dots represent PtSe$_2$ and Hf$_2$CO$_2$, respectively. The green arrow lines denote the CBM and VBM.

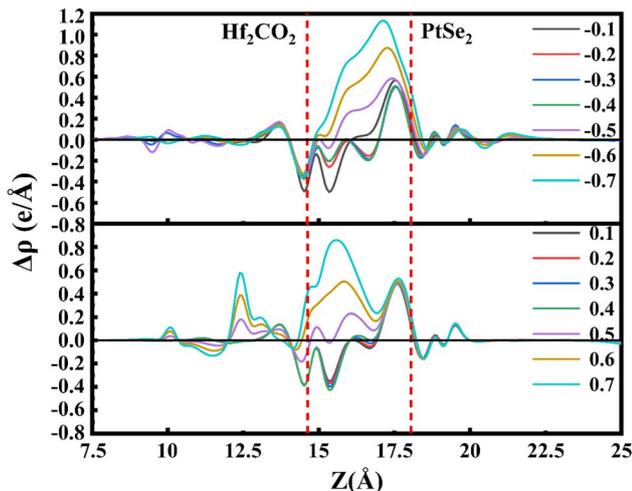© 2023 The Author(s). Published by the Royal Society of Chemistry

Fig. 7 The planar-averaged difference charge density of the PtSe$_2$/Hf$_2$CO$_2$ heterostructure with various E_{ext}.

although the PBE functional underestimates the bandgap, it is still able to predict the correct trend in bandgap variation and to properly demonstrate the physical mechanisms. Therefore, we adopted the PBE functional in the following calculations due to the high computational cost of HSE06.

The direction of E_{ext} from the Hf$_2$CO$_2$ layer to the PtSe$_2$ layer is taken as the positive direction (shown in Fig. 5a) and the E_{ext} ranging from −0.7 to 0.7 V Å^{-1} is applied. Fig. 5a and b show the band gap and band edges (VBM, CBM) as a function of the applied electric field. When the negative E_{ext} is applied, a transition from type-I to type-II occurs at −0.2 V Å^{-1}, and the band gap value decreases linearly with increasing the negative electric field. In the type-II heterostructure induced by negative electric field, the CBM and VBM are dominated by PtSe$_2$ and Hf$_2$CO$_2$ layers, respectively, as shown in Fig. 6d. Under the influence of the positive E_{ext}, the transition from type-I to type-II takes place at 0.1 V Å^{-1}. However, in contrast to the case of the negative electric field, the CBM and VBM of the type-II heterostructure are dominated by Hf$_2$CO$_2$ and PtSe$_2$, respectively, as shown in Fig. 6e. And the band gap value decreases linearly with increasing the positive electric field. The linear variations of band gaps with E_{ext} can be attributed to the Stark effect.[55]

When applying a negative E_{ext}, the total electric field is weakened due to the opposite direction of the built-in and external electric field. In this case, the drift of electrons from the Hf$_2$CO$_2$ layer to the PtSe$_2$ layer is further strengthened, resulting in a downward shift of the quasi-Fermi level of the Hf$_2$CO$_2$ layer and an upward shift of the quasi-Fermi level of the PtSe$_2$ layer, shown in Fig. 6a. As shown in Fig. 6c, when the positive E_{ext} is applied, the built-in electric field and external electric field have the same direction, and the total electric field is enhanced, causing an upward of $E_F^{Hf_2CO_2}$ and a downward of $E_F^{PtSe_2}$. The response of the electrical properties of PtSe$_2$/Hf$_2$CO$_2$ heterostructure to E_{ext} makes the PtSe$_2$/Hf$_2$CO$_2$ heterostructure exhibit potential applications in FETs and MEMS.

The distinct responses of the electronic properties of PtSe$_2$/Hf$_2$CO$_2$ heterostructure to positive and negative electric fields can be attributed to the charge transfer and redistribution between the PtSe$_2$ and Hf$_2$CO$_2$ layers. Therefore, the planar-average charge density difference of heterostructure under different E_{ext} is plotted in Fig. 7. The positive and negative values reflect electrons accumulation and depletion, respectively. It can be obviously seen that the number of accumulated electrons at the PtSe$_2$ side increases with the enhanced strength of the negative E_{ext}, while the number of depleted electrons near the Hf$_2$CO$_2$ surface decreases with the positive E_{ext} increasing from 0.1 to 0.4 V Å^{-1}, then the electrons accumulation occurs at $E_{ext} = 0.5$ V Å^{-1}, and the number of accumulated electrons increases with the enhanced strength of the positive E_{ext}.

3.4. Effect of biaxial strain

Biaxial strain has also been regarded as a powerful tool for tuning the electronic properties of 2D materials and vdW heterostructures. In this work, the electronic properties of PtSe$_2$/Hf$_2$CO$_2$ heterostructures have been investigated under a series of biaxial strains ranging from −8% to 8%, with a step of 2%. Fig. 8a depicts the strain energy (E_S), checked by $E_S = E_1 - E_0$, in which E_1 and E_0 are its total energies of strained and original structures with no strain applied, respectively. The E_S increases quadratically with strain, indicating that all strains studied are below the elastic limit and are therefore fully reversible.[54,56]

Fig. 8b and c illustrate the evolution of the bandgap and the band edges (CBM and VBM) of PtSe$_2$/Hf$_2$CO$_2$ heterostructure as a function of the strain. The two inset plots illustrate the two different type-II band alignments. One can see that the band gap of PtSe$_2$/Hf$_2$CO$_2$ heterostructure decreases with increasing the compressive strain. When the compressive strain is increased to −4%, a type-I to type-II band alignment transition takes place, and the CBM and VBM are contributed by Hf$_2$CO$_2$ layer and PtSe$_2$ layer, respectively, then a semiconductor-to-metal transition occurs when the compressive strain is increased to −8%. On the contrary, the PtSe$_2$/Hf$_2$CO$_2$ heterostructure is transformed to a type-II heterostructure when the PtSe$_2$/Hf$_2$CO$_2$ heterostructure is increase to 2%, in which the CBM and VBM are located in PtSe$_2$ layer and Hf$_2$CO$_2$ layer, respectively. To further unravel the modulation mechanism of strain effects on electronic properties of PtSe$_2$/Hf$_2$CO$_2$ heterostructure, the electronic band structures under different strains are plotted in Fig. 9. After application of −2% compressive strain, the VBM of PtSe$_2$ layer increases, closing to the VBM of Hf$_2$CO$_2$ layer. When the compressive strain is increased to −4%, the VBM of PtSe$_2$ layer continue to increase, higher than the VBM of Hf$_2$CO$_2$ layer, resulting in a type-I to type-II transition. With the compressive strain increased to −8%, the VBM of PtSe$_2$ layer is higher than the CBM of Hf$_2$CO$_2$ layer, a semiconductor-to-metal occurs. Besides, we found that the band gap of PtSe$_2$ layer increases then decreases while the band gap of Hf$_2$CO$_2$ layers decreases with increasing the compressive strain. For the tensile strain, the CBM of Hf$_2$CO$_2$ layer greatly increases at the strain of −2%, thus changes the CBM of the heterostructure from Hf$_2$CO$_2$ to PtSe$_2$ layer. As a result, a type-I to type-II transition takes place. With the increase of the tensible strain, the CBM of PtSe$_2$ layer decreases, inducing the decrease of the
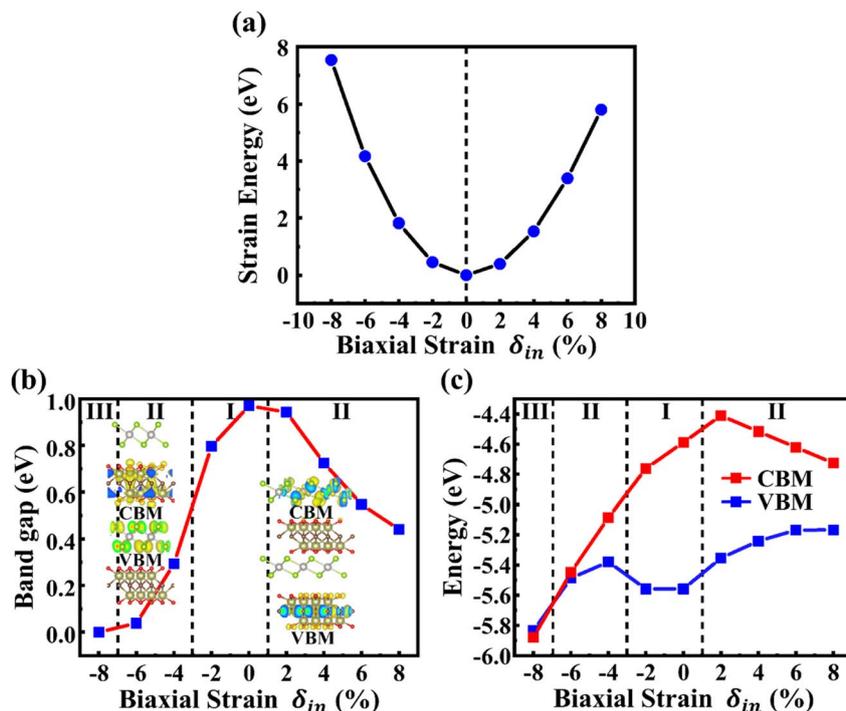
Fig. 8 (a) Strain energies at various biaxial strains ranging from −8% to 8%. (b) and (c) The band gap and band edge evolution of $PtSe_2/Hf_2CO_2$ heterostructure as a function of biaxial strains.
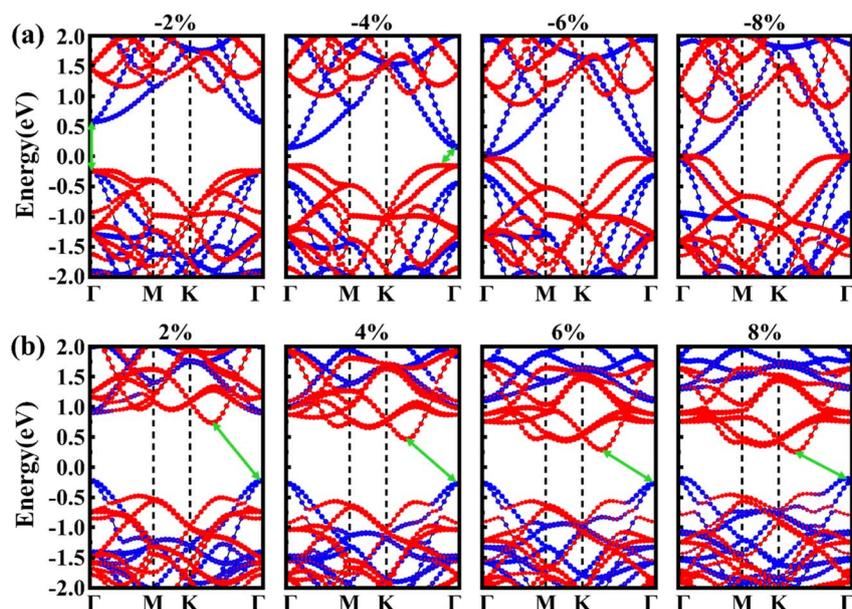
Fig. 9 (a) The electronic band structures of $PtSe_2/Hf_2CO_2$ heterostructure under compressive strains in the range of −2% to 8%. (b) The electronic band structures of $PtSe_2/Hf_2CO_2$ heterostructure under tensile strains in the range of 2% to 8%. The red circles represent the band of $PtSe_2$ layer, and the blue circles represent the band of Hf_2CO_2 layer.

bandgap of $PtSe_2/Hf_2CO_2$ heterostructure. In addition, we found that the bandgap of Hf_2CO_2 layers increases while the bandgap of $PtSe_2$ layers decreases with increasing the tensible strain.

4. Conclusions

In this work, the structural and electronic properties of $PtSe_2/Hf_2CO_2$ heterostructures have been systematically investigated

using first principles calculations. The $PtSe_2/Hf_2CO_2$ bilayer forms a stable vdW heterostructure. In equilibrium $PtSe_2/Hf_2CO_2$ heterostructures, both the CBM and VBM are donated by the Hf_2CO_2 layer, resulting in a type-I band alignment, which can be utilized in LEDs or other optoelectronic devices. It has been also demonstrated that the electronic properties of $PtSe_2/Hf_2CO_2$ vdW heterostructure are insensitive to diverse stacking patterns whereas external electric field and biaxial strain have been proved to be efficient methods for modulating the electrical properties of $PtSe_2/Hf_2CO_2$ heterostructure. Both the external electric field and biaxial strain can induce type-I to type-II band alignment transition, which facilitate the separation of photoexcited electrons and holes, enabling high efficiency optoelectronics and solar energy conversion. Furthermore, the band gap of $PtSe_2/Hf_2CO_2$ heterostructure decreases with increasing the strength of external electric field or biaxial strain after the occurrence of type-I to type-II transition. In addition, a semiconductor-to-metal transition takes place under the strong compressive strain of -8%. According to our results, the $PtSe_2/Hf_2CO_2$ heterostructure will present abundant opportunities for the application of flexible electronic and optoelectronic nano-devices.

Conflicts of interest

There are no conflicts to declare.

References

1 Q. H. Wang, K. Kalantar-Zadeh, A. Kis, J. N. Coleman and M. S. Strano, Electronics and optoelectronics of two-dimensional transition metal dichalcogenides, *Nat. Nanotechnol.*, 2012, **7**, 699–712.

2 K. Tran, G. Moody, F. Wu, X. Lu, J. Choi, K. Kim, A. Rai, D. A. Sanchez, J. Quan and A. Singh, Evidence for moiré excitons in van der Waals heterostructures, *Nature*, 2019, **567**, 71–75.

3 T. Musso, P. V. Kumar, A. S. Foster and J. C. Grossman, Graphene oxide as a promising hole injection layer for MoS2-based electronic devices, *ACS Nano*, 2014, **8**, 11432–11439.

4 K. Kośmider and J. Fernández-Rossier, Electronic properties of the MoS2-WS2 heterojunction, *Phys. Rev. B: Condens. Matter Mater. Phys.*, 2013, **87**, 075451.

5 Y. He, Y. Yang, Z. Zhang, Y. Gong, W. Zhou, Z. Hu, G. Ye, X. Zhang, E. Bianco and S. Lei, Strain-induced electronic structure changes in stacked van der Waals heterostructures, *Nano Lett.*, 2016, **16**, 3314–3320.

6 X.-H. Li, X.-H. Cui, C.-H. Xing, H.-L. Cui and R.-Z. Zhang, Strain-tunable electronic and optical properties of Zr2CO2 MXene and MoSe2 van der Waals heterojunction: a first principles calculation, *Appl. Surf. Sci.*, 2021, **548**, 149249.

7 C.-H. Lee, G.-H. Lee, A. M. Van Der Zande, W. Chen, Y. Li, M. Han, X. Cui, G. Arefe, C. Nuckolls and T. F. Heinz, Atomically thin p–n junctions with van der Waals heterointerfaces, *Nat. Nanotechnol.*, 2014, **9**, 676–681.

8 L. Britnell, R. Gorbachev, R. Jalil, B. Belle, F. Schedin, A. Mishchenko, T. Georgiou, M. Katsnelson, L. Eaves and S. Morozov, Field-effect tunneling transistor based on vertical graphene heterostructures, *Science*, 2012, **335**, 947–950.

9 J. Low, J. Yu, M. Jaroniec, S. Wageh and A. A. Al-Ghamdi, Heterojunction photocatalysts, *Adv. Mater.*, 2017, **29**, 1601694.

10 Z. Lu, D. Lockwood and J.-M. Baribeau, Quantum confinement and light emission in SiO2/Si superlattices, *Nature*, 1995, **378**, 258–260.

11 Z. Guo, N. Miao, J. Zhou, B. Sa and Z. Sun, Strain-mediated type-I/type-II transition in MXene/Blue phosphorene van der Waals heterostructures for flexible optical/electronic devices, *J. Mater. Chem. C*, 2017, **5**, 978–984.

12 R. Marschall, Semiconductor composites: strategies for enhancing charge carrier separation to improve photocatalytic activity, *Adv. Funct. Mater.*, 2014, **24**, 2421–2440.

13 G. Wang, L. Gong, Z. Li, B. Wang, W. Zhang, B. Yuan, T. Zhou, X. Long and A. Kuang, A two-dimensional CdO/CdS heterostructure used for visible light photocatalysis, *Phys. Chem. Chem. Phys.*, 2020, **22**, 9587–9592.

14 J. Na, Y. Kim, J. H. Smet, M. Burghard and K. Kern, Gate-tunable tunneling transistor based on a thin black phosphorus–SnSe2 heterostructure, *ACS Appl. Mater. Interfaces*, 2019, **11**, 20973–20978.

15 C. Tan, S. Yin, J. Chen, Y. Lu, W. Wei, H. Du, K. Liu, F. Wang, T. Zhai and L. Li, Broken-gap PtS2/WSe2 van der Waals heterojunction with ultrahigh reverse rectification and fast photoresponse, *ACS Nano*, 2021, **15**, 8328–8337.

16 X. Cong, Y. Zheng, F. Huang, Q. You, J. Tang, F. Fang, K. Jiang, C. Han and Y. Shi, Efficiently band-tailored type-III van der Waals heterostructure for tunnel diodes and optoelectronic devices, *Nano Res.*, 2022, **15**, 8442–8450.

17 H. V. Phuc, N. N. Hieu, B. D. Hoi and C. V. Nguyen, Interlayer coupling and electric field tunable electronic properties and Schottky barrier in a graphene/bilayer-GaSe van der Waals heterostructure, *Phys. Chem. Chem. Phys.*, 2018, **20**, 17899–17908.

18 K. Rahimi, Electric-field-and strain-induced adjustability of vdW heterostructure of g-ZnO/2H-TiS2 for optoelectronic applications, *Mater. Lett.*, 2021, **282**, 128680.

19 W. Guo, X. Ge, S. Sun, Y. Xie and X. Ye, The strain effect on the electronic properties of the MoSSe/WSSe van der Waals heterostructure: a first-principles study, *Phys. Chem. Chem. Phys.*, 2020, **22**, 4946–4956.

20 M. Naguib, M. Kurtoglu, V. Presser, J. Lu, J. Niu, M. Heon, L. Hultman, Y. Gogotsi and M. W. Barsoum, Two-dimensional nanocrystals produced by exfoliation of Ti3AlC2, *Adv. Mater.*, 2011, **23**, 4248–4253.

21 R. Ma, Z. Chen, D. Zhao, X. Zhang, J. Zhuo, Y. Yin, X. Wang, G. Yang and F. Yi, Ti3C2TxMXene for electrode materials of supercapacitors, *J. Mater. Chem. A*, 2021, **9**, 11501–11529.

22 O. Folorunso, N. Kumar, Y. Hamam, R. Sadiku and S. S. Ray, Recent progress on 2D metal carbide/nitride (MXene)

nanocomposites for lithium-based batteries, *FlatChem*, 2021, **29**, 100281.

23 S. Venkateshalu and A. N. Grace, MXenes—a new class of 2D layered materials: synthesis, properties, applications as supercapacitor electrode and beyond, *Appl. Mater. Today*, 2020, **18**, 100509.

24 S.-C. Zhu, S. Li, B. Tang, H. Liang, B.-J. Liu, G. Xiao and F.-X. Xiao, MXene-motivated accelerated charge transfer over TMCs quantum dots for solar-powered photoreduction catalysis, *J. Catal.*, 2021, **404**, 56–66.

25 J. Nan, X. Guo, J. Xiao, X. Li, W. Chen, W. Wu, H. Liu, Y. Wang, M. Wu and G. Wang, Nanoengineering of 2D MXene-based materials for energy storage applications, *Small*, 2021, **17**, 1902085.

26 H. Zhang, G. Yang, X. Zuo, H. Tang, Q. Yang and G. Li, Computational studies on the structural, electronic and optical properties of graphene-like MXenes (M2CT2, M = Ti, Zr, Hf; T = O, F, OH) and their potential applications as visible-light driven photocatalysts, *J. Mater. Chem. A*, 2016, **4**, 12913–12920.

27 X.-H. Zha, Q. Huang, J. He, H. He, J. Zhai, J. S. Francisco and S. Du, The thermal and electrical properties of the promising semiconductor MXene Hf2CO2, *Sci. Rep.*, 2016, **6**, 27971.

28 X. Li, Y. Dai, Y. Ma, Q. Liu and B. Huang, Intriguing electronic properties of two-dimensional MoS2/TM2CO2 (TM = Ti, Zr, or Hf) hetero-bilayers: type-II semiconductors with tunable band gaps, *Nanotechnology*, 2015, **26**, 135703.

29 Y. Zhang, R. Xiong, B. Sa, J. Zhou and Z. Sun, MXenes: promising donor and acceptor materials for high-efficiency heterostructure solar cells, *Sustainable Energy Fuels*, 2021, **5**, 135–143.

30 L. Li, H.-T. Yan and X.-H. Li, Effect of preadsorbing gas molecules on the adsorption of SO2 molecule on Hf2CO2 MXene by first-principles study, *Surf. Interfaces*, 2023, 102639.

31 J. Hao, J. Wu, D. Wang, C. Wang, M. Luo, L. Xie, F. Zhu, X. Yan and Y. Gu, Highly efficient photocatalytic overall water splitting in two-dimensional van der Waals MoS2/Hf2CO2 heterostructure, *J. Phys. D: Appl. Phys.*, 2022, **56**, 035501.

32 B. Zhu, F. Zhang, J. Qiu, X. Chen, K. Zheng, H. Guo, J. Yu and J. Bao, A novel Hf2CO2/WS2 van der Waals heterostructure as a potential candidate for overall water splitting photocatalyst, *Mater. Sci. Semicond. Process.*, 2021, **133**, 105947.

33 M. Zhang, R. Si, X. Wu, Y. Dong, K. Fu, X. Xu, J. Zhang, L. Li and Y. Guo, Two-dimensional Hf2CO2/GaN van der Waals heterostructure for overall water splitting: a density functional theory study, *J. Mater. Sci.: Mater. Electron.*, 2021, **32**, 19368–19379.

34 A. Kandemir, B. Akbali, Z. Kahraman, S. Badalov, M. Ozcan, F. İyikanat and H. Sahin, Structural, electronic and phononic properties of PtSe2: from monolayer to bulk, *Semicond. Sci. Technol.*, 2018, **33**, 085002.

35 K. Ullah, S. Ye, S.-B. Jo, L. Zhu, K.-Y. Cho and W.-C. Oh, Optical and photocatalytic properties of novel heterogeneous PtSe2–graphene/TiO2 nanocomposites

synthesized *via* ultrasonic assisted techniques, *Ultrason. Sonochem.*, 2014, **21**, 1849–1857.

36 X. Zhao, W. Niu, H. Zhang, X. Dai, S. Wei and L. Yang, Effects of interlayer coupling and electric field on the electronic properties of PtSe2/ZrSe2 van der Waals heterojunctions, *Appl. Surf. Sci.*, 2020, **510**, 145316.

37 P. Li, L. Li and X. C. Zeng, Tuning the electronic properties of monolayer and bilayer PtSe2 *via* strain engineering, *J. Mater. Chem. C*, 2016, **4**, 3106–3112.

38 C. Yim, K. Lee, N. McEvoy, M. O'Brien, S. Riazimehr, N. C. Berner, C. P. Cullen, J. Kotakoski, J. C. Meyer and M. C. Lemme, High-performance hybrid electronic devices from layered PtSe2 films grown at low temperature, *ACS Nano*, 2016, **10**, 9550–9558.

39 Z. Wang, Q. Li, F. Besenbacher and M. Dong, Facile synthesis of single crystal PtSe2 nanosheets for nanoscale electronics, *Adv. Mater.*, 2016, **28**, 10224–10229.

40 K. Ullah, S. Ye, L. Zhu, S. B. Jo, W. K. Jang, K.-Y. Cho and W.-C. Oh, Noble metal doped graphene nanocomposites and its study of photocatalytic hydrogen evolution, *Solid State Sci.*, 2014, **31**, 91–98.

41 M. Sajjad, E. M. Muñoz, N. Singh and U. Schwingenschlögl, Superior gas sensing properties of monolayer PtSe2, *Adv. Mater. Interfaces*, 2016, **4**, 1600911.

42 J. Hafner, Ab-initio simulations of materials using VASP: density-functional theory and beyond, *J. Comput. Chem.*, 2008, **29**, 2044–2078.

43 G. Kresse and J. Furthmüller, Efficient iterative schemes for *ab initio* total-energy calculations using a plane-wave basis set, *Phys. Rev. B: Condens. Matter Mater. Phys.*, 1996, **54**, 11169.

44 J. P. Perdew, K. Burke and M. Ernzerhof, Generalized gradient approximation made simple, *Phys. Rev. Lett.*, 1996, **77**, 3865.

45 S. Grimme, J. Antony, S. Ehrlich and H. Krieg, A consistent and accurate *ab initio* parametrization of density functional dispersion correction (DFT-D) for the 94 elements H-Pu, *J. Chem. Phys.*, 2010, **132**, 154104.

46 S. Han, Y. Li and Z. Wang, PtSe2/SiH van der Waals type-II heterostructure: a high efficiency photocatalyst for water splitting, *Phys. Chem. Chem. Phys.*, 2020, **22**, 17145–17151.

47 R. Momeni Feili, M. Dadsetani, R. Nejatipour and A. Ebrahimian, Electron Energy Loss Structures of Terminated Scandium and Hafnium MXene Monolayers from First-Principles Calculations, *J. Electron. Mater.*, 2020, **49**, 2502–2520.

48 X. Meng, Y. Shen, J. Liu, L. Lv, X. Yang, X. Gao, M. Zhou, X. Wang, Y. Zheng and Z. Zhou, The PtSe2/GaN van der Waals heterostructure photocatalyst with type II alignment: a first-principles study, *Appl. Catal., A*, 2021, **624**, 118332.

49 K. Ren, W. Tang, M. Sun, Y. Cai, Y. Cheng and G. Zhang, A direct Z-scheme PtS2/arsenene van der Waals heterostructure with high photocatalytic water splitting efficiency, *Nanoscale*, 2020, **12**, 17281–17289.

50 C. Fu, G. Wang, Y. Huang, Y. Chen, H. Yuan, Y. S. Ang and H. Chen, Two-dimensional CdS/SnS2 heterostructure:

a highly efficient direct Z-scheme water splitting photocatalyst, *Phys. Chem. Chem. Phys.*, 2022, **24**, 3826–3833.

51 G. Wang, F. Zhou, B. Yuan, S. Xiao, A. Kuang, M. Zhong, S. Dang, X. Long and W. Zhang, Strain-Tunable Visible-Light-Responsive Photocatalytic Properties of Two-Dimensional CdS/g-C(3)N(4): A Hybrid Density Functional Study, *Nanomaterials*, 2019, **9**, 244.

52 F. Opoku, A. Aniagyei, O. Akoto, E. E. Kwaansa-Ansah, N. K. Asare-Donkor and A. A. Adimado, Effect of van der Waals stacking in CdS monolayer on enhancing the hydrogen production efficiency of SiH monolayer, *Mater. Adv.*, 2022, **3**, 4629–4640.

53 Y. Fan, B. Yang, X. Song, X. Shao and M. Zhao, Direct Z-scheme photocatalytic overall water splitting on 2D CdS/InSe heterostructures, *J. Phys. D: Appl. Phys.*, 2018, **51**, 395501.

54 L. Fang, Y. Ni, J. Hu, Z. Tong, X. Ma, H. Lv and S. Hou, First-principles insights of electronic properties of Blue Phosphorus/MoSi2N4 van der Waals heterostructure *via* vertical electric field and biaxial strain, *Phys. E*, 2022, **143**, 115321.

55 F. Zheng, Z. Liu, J. Wu, W. Duan and B.-L. Gu, Scaling law of the giant Stark effect in boron nitride nanoribbons and nanotubes, *Phys. Rev. B: Condens. Matter Mater. Phys.*, 2008, **78**, 085423.

56 J. Wang, Y. Huang, F. Ma, J. Zhang, X. Wei and J. Liu, Strain engineering the electronic and photocatalytic properties of WS2/blue phosphene van der Waals heterostructures, *Catal. Sci. Technol.*, 2021, **11**, 179–190.